

Impact of Overpressure on the Deep Shale Pore System—A Case Study of Wufeng–Longmaxi Formations from the Southern Sichuan Basin

Lingling Xu, Renfang Pan,* Haiyan Hu,* and Tao Wang

Cite This: *ACS Omega* 2023, 8, 28674–28689

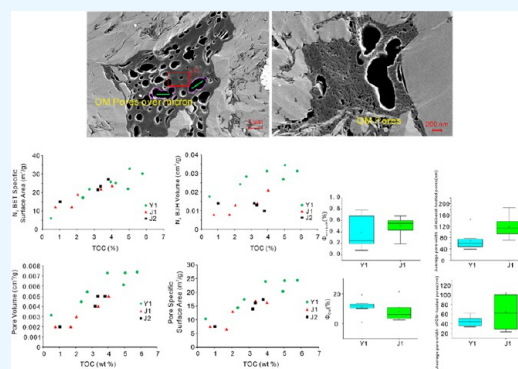
Read Online

ACCESS |

Metrics & More

Article Recommendations

ABSTRACT: This study investigated the effect of overpressure on the deep shale pore system in the Wufeng–Longmaxi Formation (WLF), a well-established shale gas reservoir in the southern Sichuan Basin, China. The Y1 well was drilled to explore deeper overpressured sections of the basin. Organic geochemistry, mineralogy analysis, field emission scanning electron microscopy (FE-SEM), and gas physisorption experiments were conducted to analyze the pore system. Results showed that despite strong compaction, deep organic-rich shale retained large pores. Compared to shallow shale, deep shale had a larger organic porosity with a smaller average pore size, although some pore sizes exceeded those in shallow shale. Nitrogen (N₂) adsorption indicated that the abundance of organic matter (OM) affected mesoporous volume and specific surface area (SSA), while carbon dioxide (CO₂) adsorption experiments suggested that micropores were not influenced by OM abundance. Comparing calculated pore SSA and volume via gas adsorption of shallower and deep shale samples revealed that, under similar OM abundance, pore SSA was nearly identical, but deep shale had a larger pore volume than shallow shale. The preservation of pores, particularly in deep shale, is attributed to overpressure, which protects against collapse; additionally, generated shale gas during thermal evolution of OM serves as pore support.



1. INTRODUCTION

Although middle-shallow (≤ 3500 m) shale gas from the Wufeng–Longmaxi Formation (WLF) in the southern Sichuan Basin has been successfully developed,^{1–4} the high productivity wells in the Luzhou area from WLF have demonstrated greater potential for deep shale (>3500 m) gas in the southern Sichuan Basin, South China,⁵ and are also expected to be the next target for shale gas exploitation.

The pore network provides gas storage space and permeability pathways for natural gases,^{6–8} which determines the potential development capacity and efficiency of shale gas wells. Organic matter (OM) pores are prevalent in black shales. To date, they have been considered the main space for shale gas accumulation.^{6,9} However, the pore size is mainly nanoscale,⁸ and microscale OM pores are rare, especially in deep shale due to strong compaction. Due to differences in resources, sediment supply, and sedimentary environments, mineral assemblages are different in gas shale, resulting in different types of initial OM and primary pores.^{10–12} Numerous OM pores occurred during thermal evolution, and diagenesis produces a variety of secondary pores.¹³ Shale pore characteristics vary greatly among different lithofacies.^{14–16} Generally, the organic-rich siliceous shale exhibits high porosity and pore volume,¹⁷ and it has been demonstrated that rigid grains like silica and pyrite can

prevent the collapse of primary pores due to compaction, which is beneficial to the expansion of storage space and the enrichment of shale gas.¹⁸ Additionally, clay minerals can affect pore volume and development.¹⁹ However, despite the fact that black shales have identical OM types, equal total organic carbon (TOC) content, similar mineral components, and comparable Ro values, high heterogeneity in shale pore systems has been discovered in several investigations.^{20–22} Furthermore, as burial depth increases, both the pore shape and arrangement alter with stronger compaction, resulting in slit-trip pores.²³ Recent research has shown that shale pore characteristics are partly determined by preservation conditions during the burial and uplift process, as well as various periods of tectonic deformation.^{20,24}

Compared with the successfully developed Jiaoshiba shale play with a pressure coefficient of 1.55–1.74,^{25,26} the Luzhou area is unique because its pressure coefficient is over 2.0.¹

Received: May 14, 2023

Accepted: July 12, 2023

Published: July 27, 2023



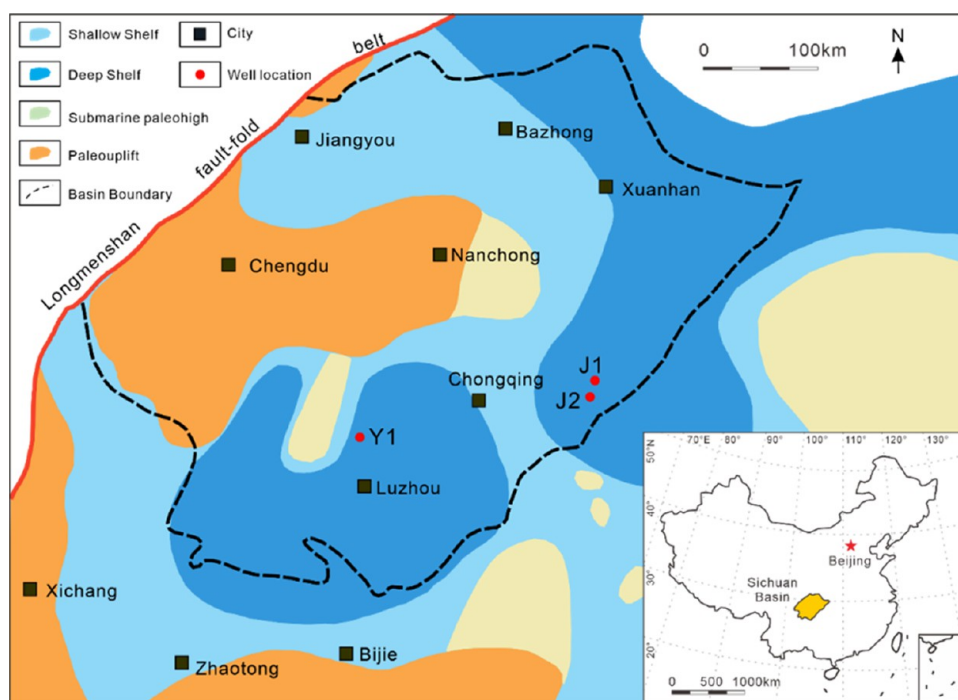


Figure 1. Sedimentary facies of the studied area during the Late Ordovician to the Early Silurian (adapted from Nie et al.).³³ The samples investigated in this paper are both deposited in a deep shelf but within different pressure coefficients.

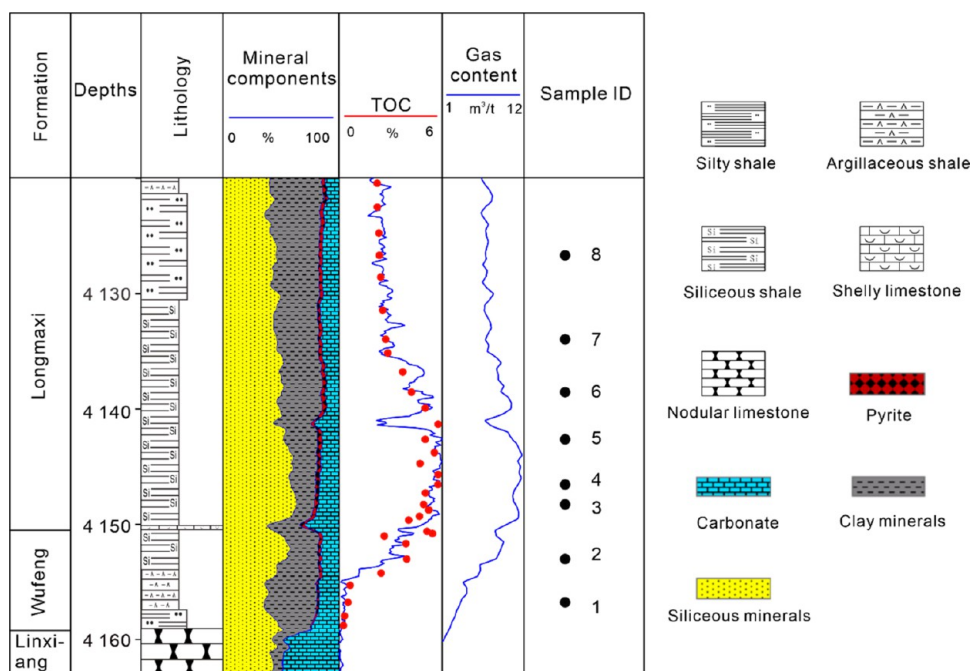


Figure 2. Lithology, mineral components, TOC, and the samples' location in well Y1.

Overpressure shale reservoirs have higher porosity than normal-pressure or low-pressure shales,^{27,28} indicating that overpressure has the ability to preserve pore structures by offsetting the stress of the overlying strata. Numerous studies have been made for middle-shallow shales in the southern Sichuan Basin, and it was found that micropores and mesopores contribute most to gas storage and correlate with TOC content and clay minerals.^{17,29} Since there are differences in geologic characteristics between shales in the Jiaoshiba area and the Luzhou area (e.g., production potential and pressure coefficient),^{1,26} their pore systems would

be different. This paper aims to (1) document the architecture of the pore system and pore types in deep shale, (2) elucidate how shale composition affects the pore system, and (3) highlight the implication of overpressure on the pore system in deep shale by comparing the shale pore structure parameters from the Luzhou area and the Jiaoshiba area under different pressure conditions.

2. GEOLOGICAL SETTING

Since the late Ordovician, the Upper Yangtze Sea, as a result of the collision between the Yangtze Block and the Cathaysia

Table 1. Bulk Rock Composition of the Deep Shale in the Studied Area for Scanning Electron Microscopy (SEM) and Gas Physorption^{a,b}

well	sample ID	depth (m)	TOC (wt %)	Ro ^c (%)	quartz	feldspar ^c	carbonate ^d	pyrite	total clays	chlorite	illite
Y1	8	4124.27	2.34	n/a	38.8	12	17.2	1.1	31	3.72	27.28
Y1	7	4131.55	2.71	3.16	43.8	7.5	11.8	1.7	35.1	n/a	n/a
Y1	6	4136.13	4.23	n/a	60.5	3.7	6.5	1.9	27.5	1.68	26.32
Y1	5	4140.22	5.04	3.04	68.1	3.2	7.2	2.1	19.3	n/a	n/a
Y1	4	4144.14	5.78	3.02	60.4	2.7	20.6	2.2	14.2	n/a	n/a
Y1	3	4145.86	4.94	n/a	61.5	2.1	24.2	1.2	11	0	11.00
Y1	2	4150.6	3.95	3.11	60	3.8	5.1	0	31.1	2.48	28.52
Y1	1	4154.35	0.495	n/a	35.7	4.4	15.6	0	44.3	n/a	n/a
J1	JY1-1	2334.89	1.34	3.32	30.5	11.2	n/a	4.3	54.0	n/a	n/a
J1	JY1-2	2348.50	1.57	n/a	31.0	13.0	2.0	1.0	53.0	n/a	n/a
J1	JY1-3	2330.86	1.15	n/a	25.2	8.7	n/a	3.5	62.6	n/a	n/a
J1	JY1-4	2343.12	2.93	3.44	31.7	11.5	21.9	3.6	31.3	n/a	n/a
J1	JY1-5	2348.83	1.82	3.24	27.3	10.2	9.9	4.8	47.8	n/a	n/a
J1	JY1-6	2384.01	3.66	n/a	41.5	9.2	12.1	4.9	32.3	n/a	n/a
J1	JY1-7	2388.59	3.66	3.09	48.5	7.1	13.3	3.9	27.2	n/a	n/a
J1	JY1-8	2404.12	4.91	n/a	46.3	9.8	10.6	5.2	28.1	n/a	n/a
J1	JY1-01	2334.39	0.75	3.22	29.8	7.6	0	0	61.1	3.05	34.22
J1	JY1-03	2371.00	1.70	2.91	28.9	12.1	16.7	0	40.5	2.03	22.67
J1	JY1-04	2382.56	2.05	3.38	40.4	8.5	8.5	0	39.3	3.14	26.33
J1	JY1-06	2401.76	3.38	n/a	53.0	7.4	9.9	0	26.7	0.53	4.01
J1	JY1-08	2411.80	4.03	3.69	69.1	3.2	6.1	0	18.3	0.36	2.75
J2	JY11-4-01	2303.64	1.02	n/a	36.0	11.1	10.9	5.9	36.1	13.36	7.22
J2	JY11-4-02	2329.62	3.20	n/a	42.3	8.9	8.9	7.7	32.2	7.73	6.76
J2	JY11-4-03	2347.78	3.35	2.98	51.5	7.6	9.0	4.8	27.1	4.60	10.30
J2	JY11-4-04	2360.02	3.80	3.22	55.5	7.9	3.1	0	33.5	5.70	10.71

^aTOC = total organic carbon content; Ro* = equivalent vitrinite reflectance calculated from the reflectance of bitumen (Rb), Ro* = 0.938Rb + 0.3145;³⁸ n/a = samples with no available data; total clays = chlorite + illite. ^bData of wells J1 and J2 were obtained from the previous studies.^{17,37,39} ^cFeldspars = orthoclase + plagioclase. ^dCarbonates = calcite + dolomite.

Block,^{30,31} has been characterized by a complex tectonic system consisting of a deep shelf basin separated by sedimentary depressions and submarine paleohigh structures. The Luzhou shale play is located in the southern part of the Sichuan Basin on the Upper Yangtze Block (Figure 1). The studied area is located in a low-steep structure that experienced slight tectonic uplift in the later period.^{32,33} Additionally, published information indicates that the pressure coefficient of the WLF in the southern Sichuan Basin increases with buried depth (Figure 1), and the Luzhou area is one of the highest parts.^{1,34}

The WLF, which was deposited in a deep shelf among the Chuanzhong paleouplift, Qianzhong paleouplift, and Xuefeng paleouplift from the Katian to Aeronian period and was dominated by the dysaerobic to anoxic environment,³⁵ is a set of black silica-rich shale (Figure 2). The mineral components were predominated by quartz and clays, followed by carbonates and pyrite, and were deposited in a marine shelf environment.³⁶

3. MATERIALS AND METHODS

This paper examines and discusses samples from well Y1 (Figure 1 and Table 1), which represent a pore system under overpressure conditions and were collected from a deep shale gas well (Y1) drilled in the Luzhou area of southern Sichuan, South China (Figure 1). All samples were selected from the target intervals scattered among the WLF in descending order of depth (Figure 2). The eight-core samples differ in lithology, with a fine-grained clay-rich layer referred to as the low Wufeng Formation, a biosiliceous-rich layer referred to as the low Longmaxi black shale, and a coarser-grained quartz-rich layer referred to as the siltstone in the upper Longmaxi Formation.

Additionally, this paper compares the data of shale pores from wells J1 and J2 in a lower pressure area (e.g., Jiaoshiba play) obtained from the published research^{17,37} with the data from well Y1 (Table 1). It should be noted that to ensure that the variables in the comparative analysis are as single as possible, we choose the same strata of the same age for comparison.

3.1. Geochemistry and Mineralogy. Forty samples were obtained from well Y1 for petrographic analysis. X-ray

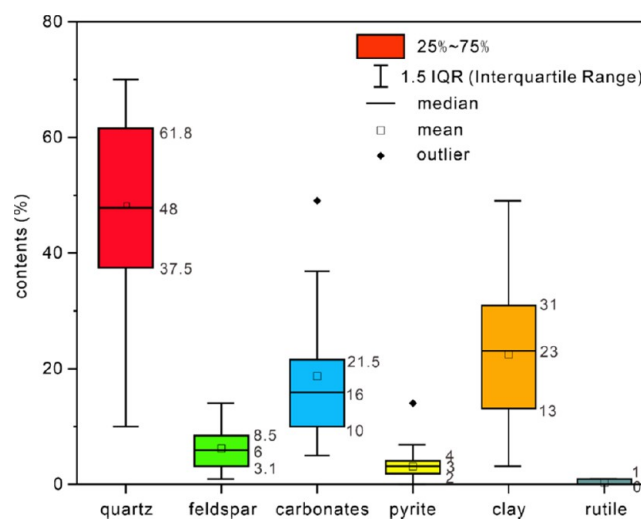


Figure 3. Box plot for the mineral composition of the Wufeng–Longmaxi Formation from well Y1. Data were determined by XRD from 40 samples.

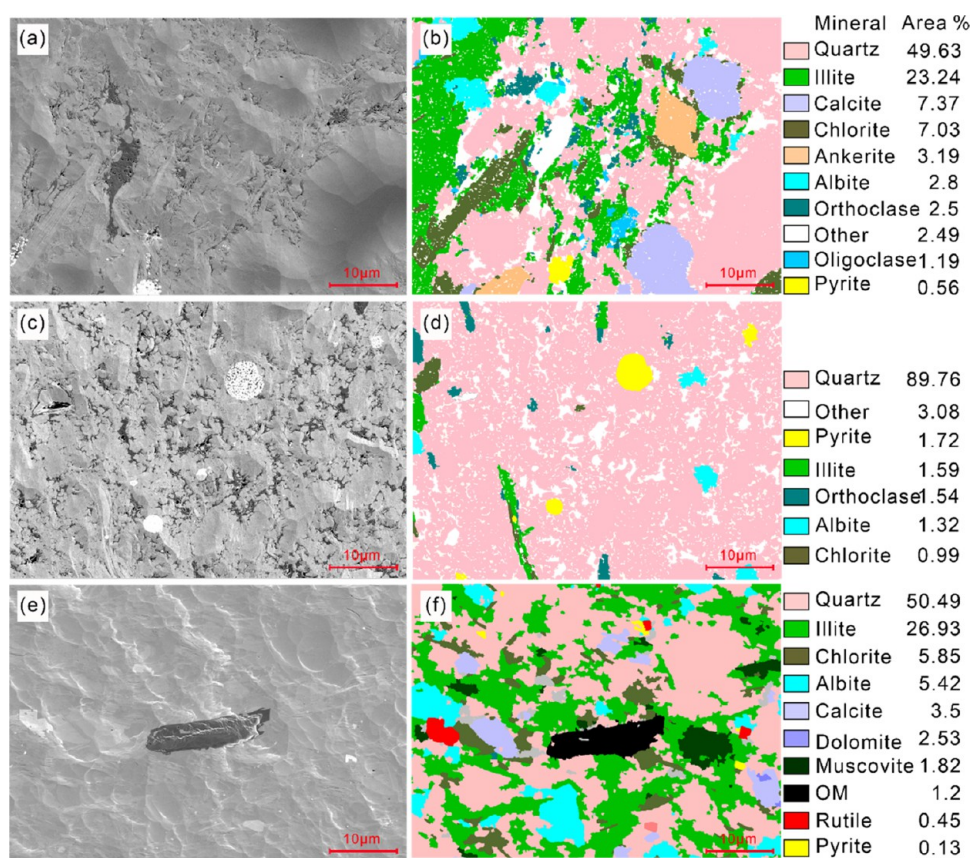


Figure 4. Mineral compositions obtained by AMICS and pore distribution acquired from the corresponding FE-SEM image. Left: FE-SEM images. Right: distribution of mineral compositions from the same sample of the left FE-SEM images. OM = organic matter. (a, b) Sample ID = 8, most pores are within organic matter, then between the mineral matrix. (c, d) Sample ID = 5, pores mainly occurred in organic matter, then the edge of quartz grains. (e, f) Sample ID = 1, little or no organic matter is observed.

diffraction (XRD) was used to analyze the bulk mineralogical composition, while four samples were analyzed for clay mineral components for diagenesis analysis. Each sample was finely milled to less than 40 μm . The bulk sample mounts were measured using $K\text{-}\alpha$ radiation on an X' Pert3 Powder diffractometer.

The TOC content of the shale samples was obtained using a LECO carbon–sulfur analyzer (CS230). About 1 g of the shale samples were pretreated with acid for over 2 h at 60–80 $^{\circ}\text{C}$ to get rid of carbonate minerals. The samples were then rinsed with distilled water and oven-dried for approximately 8 h at 60–80 $^{\circ}\text{C}$ before the TOC analysis.

To compensate for the lack of vitrinite particles in sedimentary rocks deposited before the Devonian period, the solid bitumen (Rb) reflection was measured.³⁸ The equivalent vitrinite reflection was calculated using the function $R_{\text{O}^*} = 0.938R_{\text{b}} + 0.3145$.³⁸ The reflection of solid bitumen was determined using a Zeiss Axio Scope A1 reflected-light microscope with a J&M MSP 200 microscope photometer.

3.2. Scanning Electron Microscopy Imaging. Eight samples were selected from well Y1 to represent the variation in buried depth. Field emission SEM (FE-SEM) equipped with an Automated Mineral Identification and Characterization System (AMICS) was used to determine the types and morphology of shale pores and elucidate the control of OM and minerals on pore development. AMICS analyses were also conducted for mineral identification. The imaging provided important information on lithologic variation and mineral

distribution. All samples were prepared by Ar-ion milling to create a flatter surface.⁶ Image-based parameters, such as pore width and equivalent circular diameter, of OM pores were measured by JMicroVison, and the image-based porosity was determined by point counts of FE-SEM images.

3.3. Low-Pressure Gas Physisorption Experiments. In low-pressure gas physisorption experiments, all samples were ground into about 35 mesh and then degassed under vacuum for 10 h at 120 $^{\circ}\text{C}$ to remove volatiles prior to the experiments. The experiments were conducted using a Quantachrome Autosorb iQ instrument. N_2 physisorption experiments were performed at -195.8 $^{\circ}\text{C}$, and the adsorbed volume of N_2 was determined at a specific pressure through a four-stage gradual increase process. The measurable pore sizes of low-temperature N_2 adsorption ranged from 0.35 to 500 nm. Carbon dioxide (CO_2) adsorption experiments were carried out at 0 $^{\circ}\text{C}$ with the same instrument, and the measurable pore width ranged from 0.3 to 1.5 nm. The pore structure parameters of micropores were calculated by the density functional theory (DFT) method for adsorption over relative pressure ranging from 0.0001 to 0.032.

The distributions of pore specific surface area (SSA) and pore volume were obtained from the Brunauer–Emmett–Teller (BET) method,⁴⁰ Barrett–Joyner–Halenda (BJH) model,^{41,42} and density functional theory (DFT).⁴³ The BET surface area was calculated by seven points of a relative pressure between 0.05 and 0.2 based on the BET equation.⁴⁴ This theory posits that the physical adsorption between solids and gases is caused by van der Waals forces.^{45,46} Van der Waals forces also exist

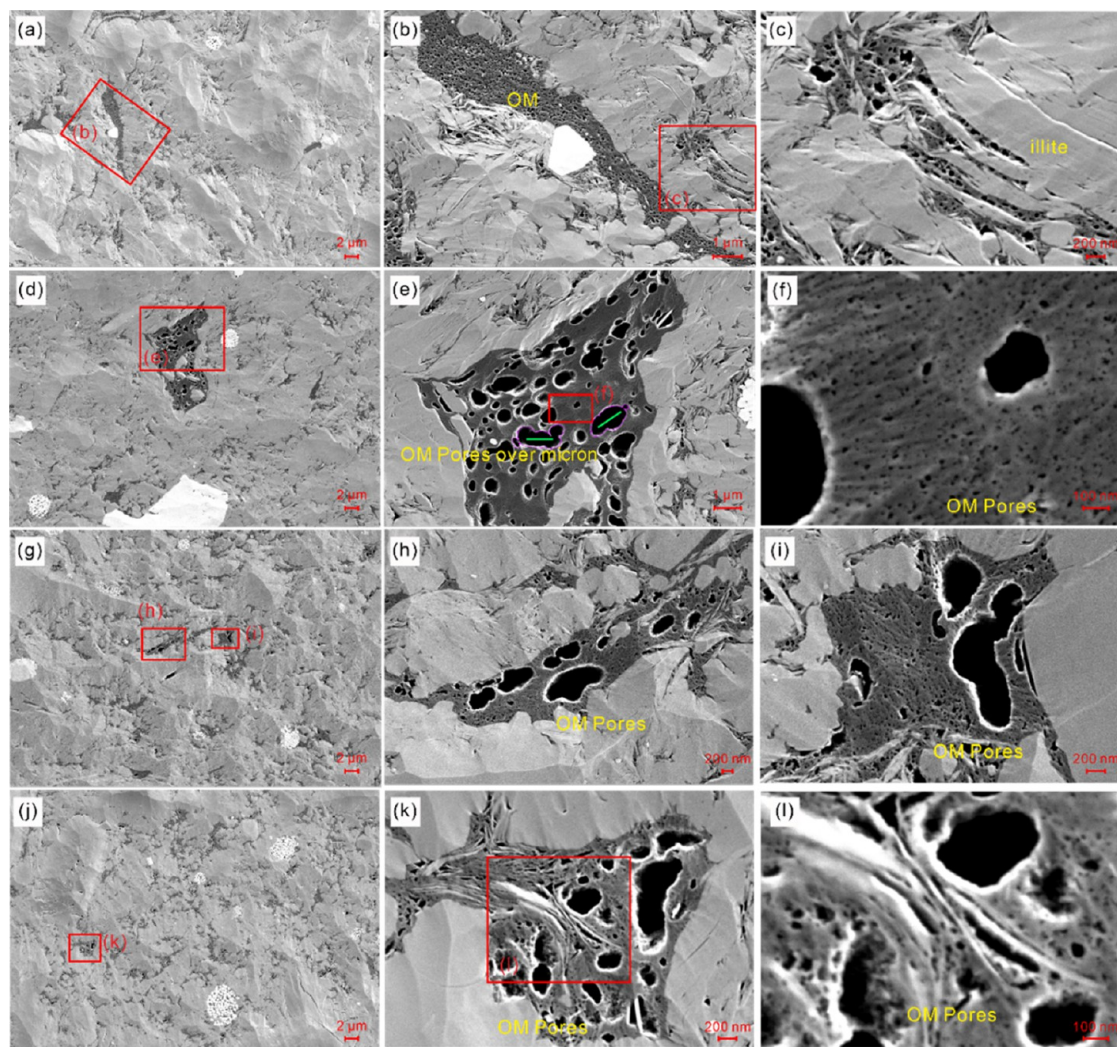


Figure 5. Macropores within OM from well Y1. (a), (d), (g), and (j) Samples in ascending order in depth with TOC content increasing, the OM was scattered among mineral matrix, and when the TOC content increases to a certain amount, the OM seems to connect by slit channels. (a) Sample ID = 8, FE-SEM photograph at a large scale. (b) Intraparticle pores within organic matter at higher magnification. (c) OM pores between clay minerals at magnification and increased resolution. (d) Sample ID = 7, macropores appear in this image. (e) Macropores developed within OM, and their outlines are drawn with a purple curve. The length of the short line with blue color is 1 μm . (f) Micropores like honeycombed or sponges developed within OM at higher magnification. (g) Sample ID = 6. (h, i) OM pores with pore sizes up to hundreds of nanometers. (j) Sample ID = 5. (k, l) Convoluted OM pores.

between gas molecules; thus, gas molecules can be adsorbed onto adsorbed molecules, forming multilayer structures. The BJH model is predicated upon the Kelvin equation and describes capillary condensation phenomena within cylindrical or spherical pores.⁴¹ It is applicable for analyzing mesoporous and macroporous pore size distributions. DFT is a typical quantum mechanical method that quantifies the interaction between an adsorbate and an adsorbent through chemical means and simulates the macroscopic adsorption properties of gases by adsorbents.^{42,43}

4. RESULTS

4.1. Petrography and Geochemistry. The results of equivalent vitrinite reflection, mineral composition, and TOC content are listed in Table 1, and the mineral composition of all samples is also summarized in a box plot (Figure 3). All samples' equivalent vitrinite reflection (R_o^*) ranges from 3.02 to 3.16% with a mean value of 3.08%. The TOC content varies dramatically with 0.495% at the bottom and up to 5.78% at

the low Longmaxi shale (Figure 2). The box plot of the mineral composition of these 40 samples obtained from XRD exhibits that quartz and clay minerals are the majority. The quartz content ranges from 10 to 70% but mainly between 37.5 and 61.8%. The clay content ranges from 3 to 49%. In addition, the mineral composition is moderate in carbonate content and low in feldspar and pyrite. The result of the clay mineral composition analysis of the selected four samples shows that no illite/smectite mixed layers exist but a number of illite layers and few chlorites (Table 1). The AMICS offered mineralogical information on the 2D surface of the deep shale (Figure 4). The sample with the highest clay minerals shows few OM pores in FE-SEM images (Figure 4c).

4.2. Morphology and Types of Deep Shale Pores. Research over the last 10 years has demonstrated multiple pore types and proposed different methods of pore classification in shale.^{6,47,48} Based on the research of Loucks,⁶ this paper further summarizes the morphology of different types of pores. After a detailed petrographic and FE-SEM study of the eight samples,

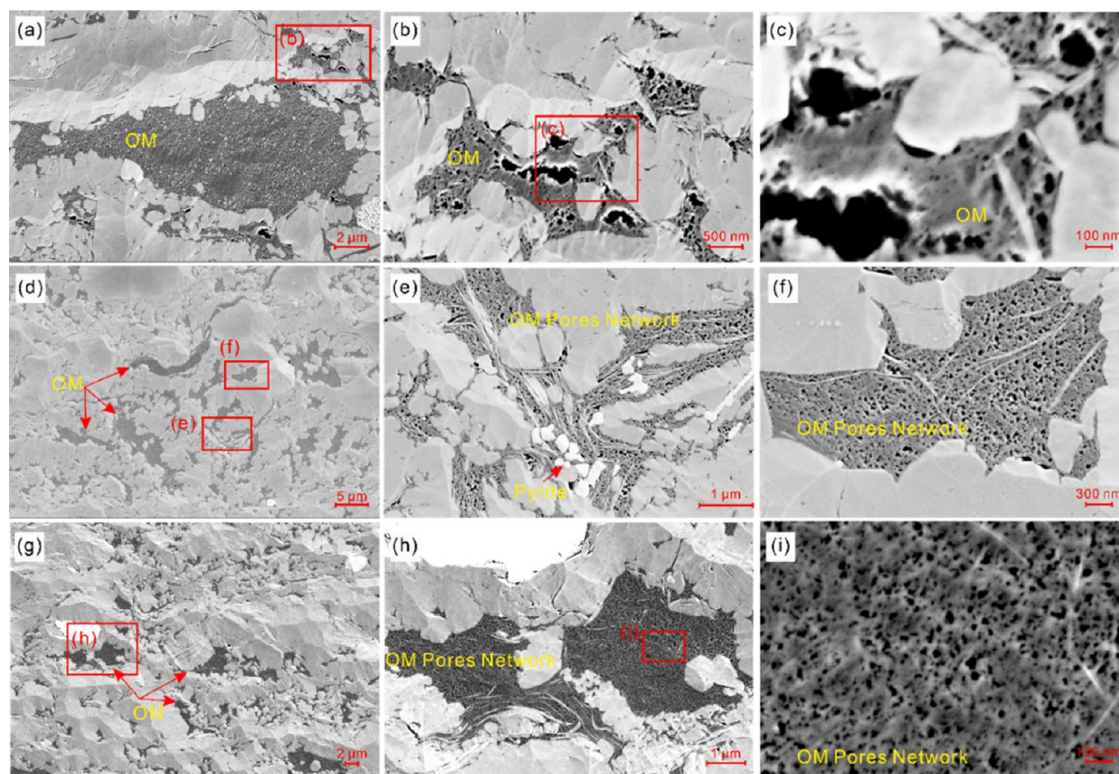


Figure 6. Mesopores and micropores in OM from well Y1. (a), (d), and (g) Samples in ascending order in depth with TOC content decreasing. (a) Sample ID = 4, individual pyrite grains scattered within organic matter. (b) Irregular OM pores. (c) OM pores between mineral grains at magnification and increased resolution. (d) Sample ID = 3, organic matter extends along the edge of mineral grains, indicating strong compaction. (e) Organic matter is intertwined with pyrite and clay minerals. (f) OM pores with almost uniform size. (g) Sample ID = 2. OM pores seem to be smaller than those in sample 3. (h, i) Micropores like honeycombs or sponges developed at higher magnification.

Table 2. Image-Based Parameters of OM Pores Measured by JMicroVison^a

well	sample ID	Φ_{\min} (%)	pore width of mineral-hosted pores (nm)			Φ_{OM} (%)	pore width of OM-hosted pores (nm)		
			max	min	average		max	min	average
Y1	8	0.79	688.49	13.03	73.23	10.03	413.06	4.82	47.31
Y1	7	0.59	518.43	11.33	54.71	12.06	1031.00	4.52	41.77
Y1	6	0.77	221.77	5.95	38.95	10.58	807.74	4.82	33.05
Y1	5	0.17	920.67	10.17	76.92	12.25	930.47	4.82	61.86
Y1	4	0.23	472.12	11.61	63.22	12.23	548.09	4.89	52.12
Y1	3	0.08	345.85	1.88	56.27	13.67	281.06	1.02	33.75
Y1	2	0.26	350.33	16.63	42.10	19.36	1704.97	5.00	38.18
Y1	1	0.22	654.34	26.63	143.98	0.94	175.52	0.14	50.27
J1	JY1-1	0.57	1137	7	103	2.40	105	7	24
J1	JY1-2	0.68	2727	13	131	3.23	434	7	34
J1	JY1-3	0.53	1323	10	70	6.72	310	3	23
J1	JY1-4	0.37	1901	6	125	21.54	948	6	104
J1	JY1-5	0.61	932	10	185	11.38	628	5	64
J1	JY1-6	0.49	491	4	96	4.16	415	8	97
J1	JY1-7	0.19	809	11	142	5.80	520	10	105
J1	JY1-8	0.59	1505	12	90	10.06	389	7	61

^aThe data of well J1 were acquired from the previous study;¹⁷ $\Phi_{\text{min-bulk}}$ = mineral-hosted porosity in the bulk rock measured by FE-SEM; Φ_{OM} = OM-hosted porosity detected by FE-SEM.

OM-hosted pores and inorganic pores were described and classified in the deep shale samples from the Luzhou area.

4.2.1. OM Pores. Results from FE-SEM images indicate that the OM-hosted pore sizes are mainly within nanometers. They are found within grains of OM (Figures 5–7), which routinely appear between mineral grains. There are partly large OM-hosted pores existing in deep shales with pore sizes over 1 μm

(Figure 5e). Some OM-hosted pores show to be cluttered at low magnification (Figures 5a,d,g,j and 6d,g).

4.2.2. Inorganic Matter Pores. Inorganic matter pores consist of interparticle (abbreviated as “interP”) pores and intraparticle (abbreviated as “intraP”) pores.⁶ The interP pores mainly occur between quartz grains, illite grains, and dolomite grains, with few found in pyrite framboids (Figure 8b,c,e). The intraP pores

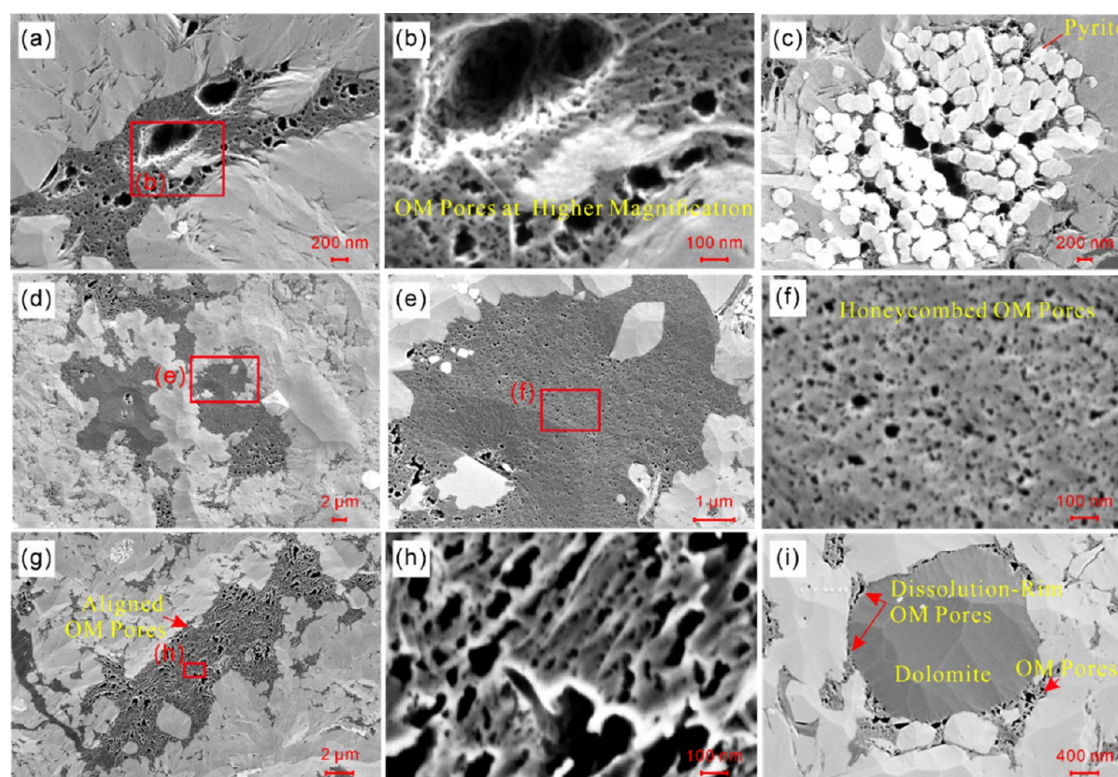


Figure 7. Special OM pores from well Y1. (a–c) Sample ID = 6, (a) OM in the mineral matrix, developed OM pores from micro- to macropores, and the inner wall of OM pores is rather rough (b), which greatly increases the adsorption sites of methane. (c) Pyrite particles dispersed in OM and developed mesopores, which preserved well from compaction, possibly because of overpressure. (d–f) Sample ID = 5, which shows the micropores within OM. (g, h) Sample ID = 4, the direction of the long axis of the OM pores is oriented, and micropores to macropores can be observed at higher magnification (h). (i) Sample ID = 3, OM pores along unstable minerals.

Table 3. Results of Pore Volume and SSA by BET, BJH, and DFT Models^a

well	sample ID	N ₂ BET surface area (m ² /g)	N ₂ DFT surface area (m ² /g)	N ₂ BJH volume (cm ³ /g)	N ₂ DFT volume (cm ³ /g)	CO ₂ DFT surface area (m ² /g)	CO ₂ DFT volume (cm ³ /g)
Y1	8	16.611	17.259	0.024	0.024	14.406	0.0044
Y1	7	19.59	21.756	0.028	0.028	17.392	0.0054
Y1	6	22.904	25.133	0.022	0.029	n/a	n/a
Y1	5	27.638	32.868	0.026	0.034	24.255	0.0073
Y1	4	25.13	30.277	0.029	0.031	24.371	0.0074
Y1	3	19.061	21.926	0.022	0.027	20.314	0.0061
Y1	2	23.766	25.694	0.031	0.031	23.936	0.0073
Y1	1	6.815	6.137	0.019	0.018	10.342	0.0031
J1	JY1-01	12.18	n/a	0.008	n/a	7.57	0.002
J1	JY1-03	12.17	n/a	0.008	n/a	6.51	0.002
J1	JY1-04	18.88	n/a	0.013	n/a	13.03	0.003
J1	JY1-06	21.83	n/a	0.014	n/a	16.67	0.004
J1	JY1-08	23.58	n/a	0.021	n/a	16.22	0.005
J2	JY11-4-01	14.88	n/a	0.014	n/a	7.54	0.002
J2	JY11-4-02	21.52	n/a	0.014	n/a	13.95	0.004
J2	JY11-4-03	23.27	n/a	0.013	n/a	16.09	0.005
J2	JY11-4-04	27.06	n/a	0.010	n/a	17.36	0.005

^an/a = samples with no available data. The data for wells J1 and J2 were acquired from the previous study.³⁷

mainly include three types of mineral matrix pores: (1) those developed within clay minerals (Figure 8b,d,g,i), (2) those within pyrite framboids that serve as intercrystalline pores (Figure 8d,h), and (3) intraP pores within carbonate grains (Figure 8a,f). Pores between clay layers and microfractures formed by compaction and diagenesis commonly show a slit shape (Figure 8b,d,g,i). IntraP pores are routinely found in the feldspar and carbonates, in an elliptical shape (Figure 8a,f).

Pyrites observed in well Y1 are developed in clusters under FE-SEM or presented as strawberry-like crystals, forming intercrystalline pores (Figure 8d,h). InterP pores between mineral grains are in straighter polygonal shapes compared to OM pores, which have smoother edges. Meanwhile, intraP pores developed within carbonate particles are abundant and relatively small in size (Figure 8a,f).

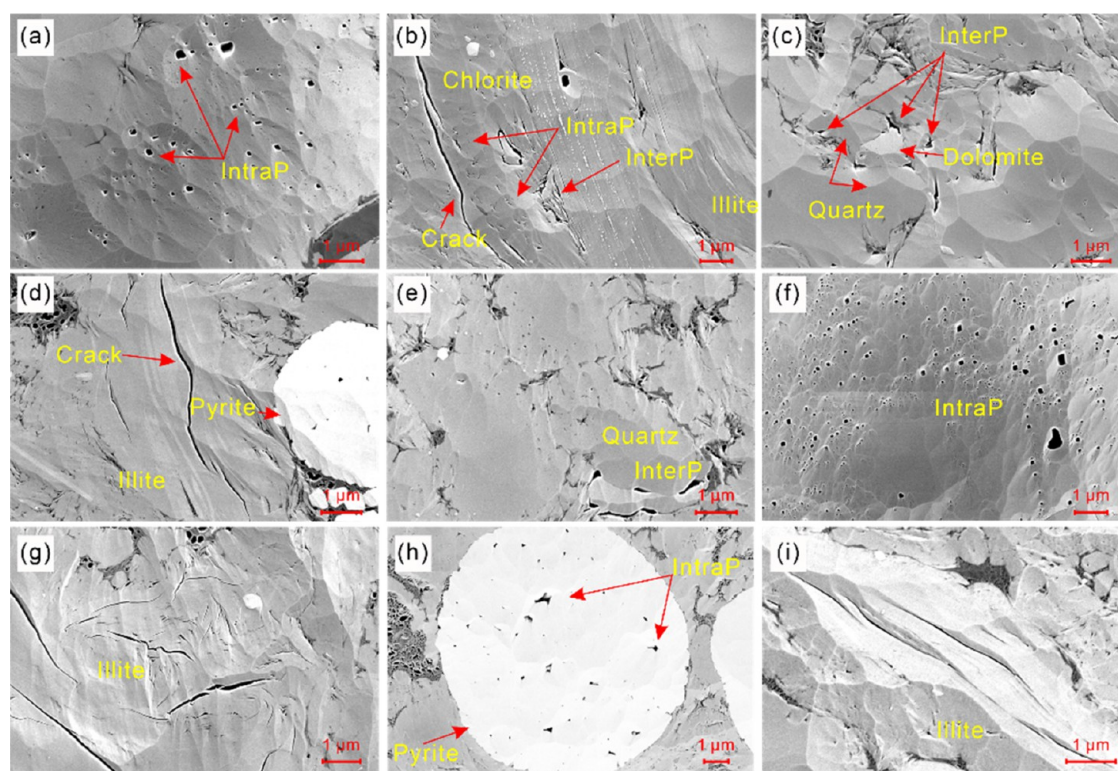


Figure 8. Typical examples of mineral matrix pores from well Y1. (a–c) Sample ID = 8, (a) dissolution pores with smooth edges, (b) cracks between chlorite and illite, (c) interP developed among rigid grains like quartz and dolomite. (d) Sample ID = 7, slightly larger microcracks in illite. (e) Sample ID = 6. InterP between quartz grains. (f) Sample ID = 4, intraP pores in dolomite grains. (g) Sample ID = 6, slit pores within illite grains. (h) Sample ID = 4, intercrystalline pores within pyrite framboids. (i) Sample ID = 2, slit pores within clays.

4.3. Pore Architecture Characterization. **4.3.1. Pore Size and Image-Based Porosity.** The results of pore size and image-based porosity calculations for OM pores are presented in Table 2. The pore width mainly ranges from 0.14 to 1704.94 nm. However, the sample with the highest TOC content does not mean that the largest pores can be observed (Table 2). The results calculated by JMicroVison show that the OM pores in sample 2 are the largest, but the TOC content of sample 2 is not the highest (Tables 2 and 3).

4.3.2. Low-Pressure CO₂ Gas Physisorption. Following the standards of the IUPAC,⁴⁹ the low-pressure CO₂ adsorption isotherms (Figure 9) belong to type I isotherms. The results of the maximum adsorbed volume, pore SSA, and pore volume obtained from the DFT model are shown in Table 3. The maximum adsorbed volume of CO₂ gas for all samples varies from 0.997 to 2.322 cm³/g, of which a clay-rich sample has the lowest CO₂ adsorption amount (Figure 9, sample ID = 1). The dV/dW and dS/dW versus pore width show similar characteristics (Figure 10a,b). Both plots of dV and dS show trimodal distributions of pore widths in the 0.3–0.9 nm range (the three peaks of pore width are 0.35, 0.5, and 0.8 nm), suggesting that those pores have relatively higher pore SSA and volume than others (Figure 10a,b). Therefore, the pore widths in the ranges of approximately 0.35, 0.44–0.7, and 0.75–0.9 nm contribute the most to the pore structure parameters.

4.3.3. Low-Temperature N₂ Gas Physisorption. The morphology of the low-temperature N₂ adsorption and desorption isotherms (Figure 11) shows similar characteristics, indicating a type IV isotherm without saturation at the end. This suggests that N₂ adsorption has not reached saturation due to the presence of larger pores or nano-micron-scale cracks in the

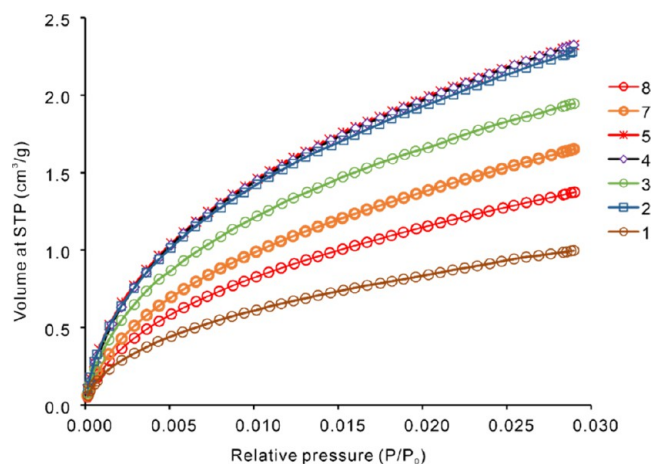


Figure 9. Low-pressure CO₂ adsorption isotherms show that the adsorption volume increases with the TOC content. However, the sample with the highest clay content and the lowest TOC content has the lowest CO₂ adsorptive volume.

samples. All isotherms exhibit a rapid increase in adsorption volume when P/P_0 is less than 0.01, indicating the presence of micropores and completion of monolayer adsorption in an extremely short time. Adsorption isotherms reflect monolayer to multilayer adsorption with a pore size smaller than 4 nm at P/P_0 less than 0.45.⁵⁰ There is no adsorption saturation at the maximum relative pressure, indicating that adsorption occurred in slit pores or parallel plate holes at this stage.

According to the IUPAC classification scheme,⁴⁹ the isotherms of all samples are close to the H3 near the saturated

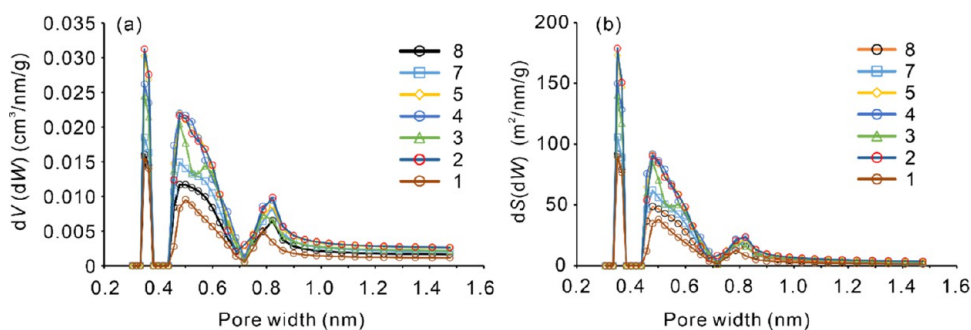


Figure 10. Pore size distribution obtained from low-pressure CO₂ adsorption isotherms appears to be trimodal, with peaks at 0.35, 0.5, and 0.8 nm. (a) Pore volume distribution versus pore width. (b) Pore SSA distribution versus pore width.

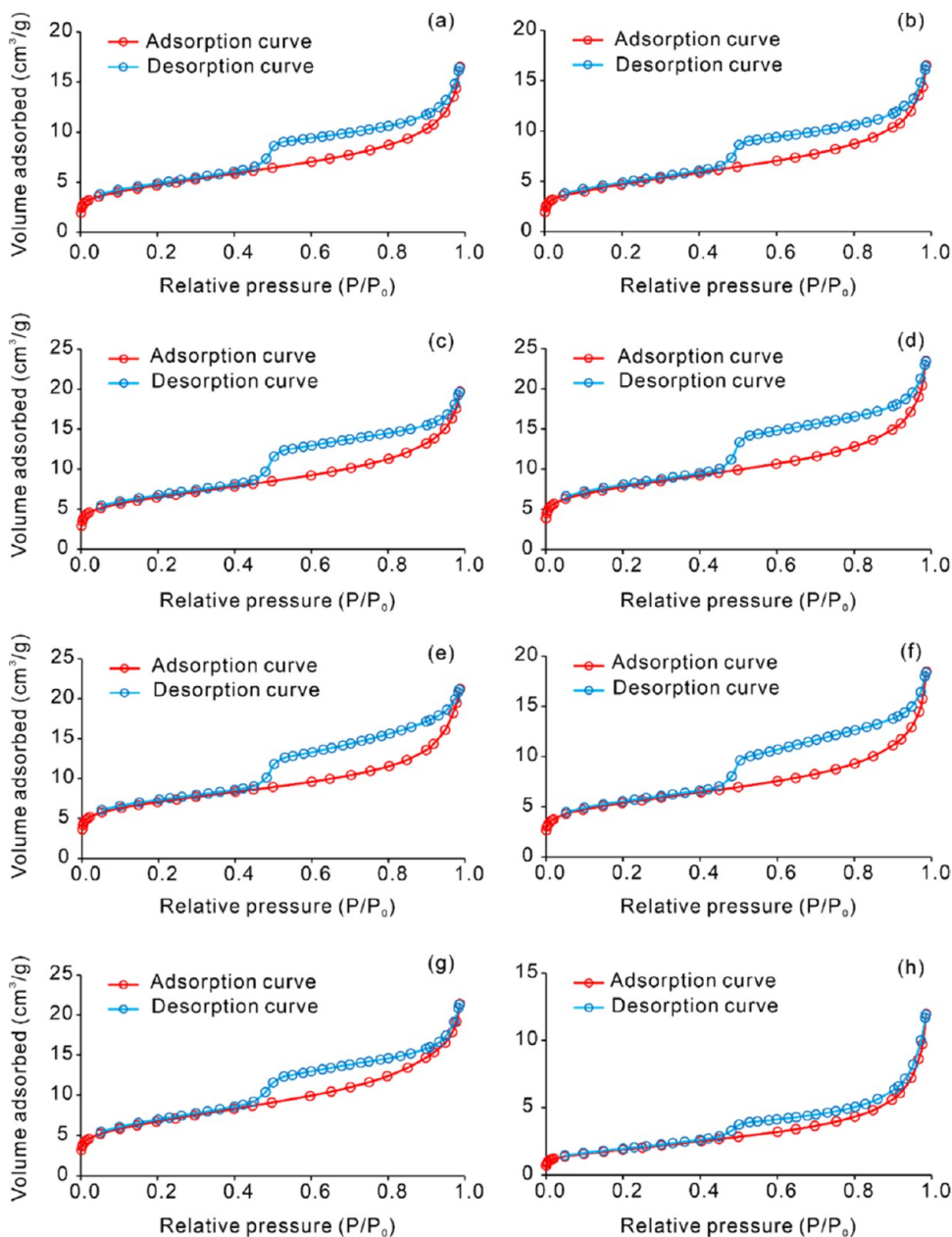


Figure 11. Adsorption and desorption isotherms via nitrogen gas for shale samples from well Y1. (a) Sample ID = 8. (b) Sample ID = 7. (c) Sample ID = 6. (d) Sample ID = 5. (e) Sample ID = 4. (f) Sample ID = 3. (g) Sample ID = 2. (h) Sample ID = 1. Among them, the higher the TOC content, the larger the hysteresis loop area.

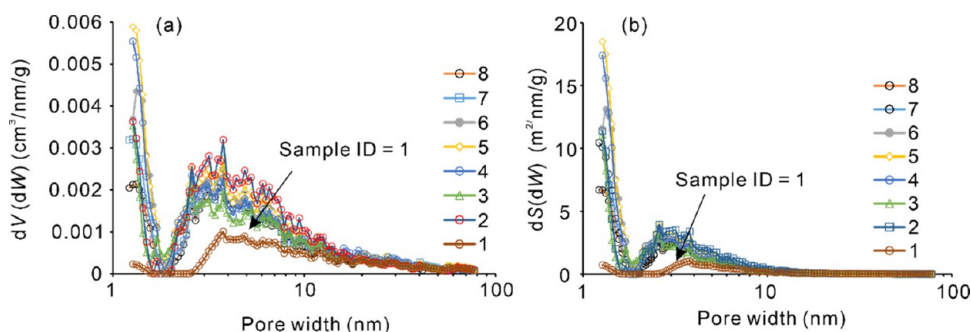


Figure 12. Pore size distribution obtained from N_2 adsorption isotherms. (a) Pore volume distribution versus pore width. (b) Pore SSA versus pore width. Both dV/dW and dS/dW plots show a unimodal distribution of pore size. However, sample 1 shows a different manner, the pore width becomes larger, but the pore volume and pore SSA become smaller.

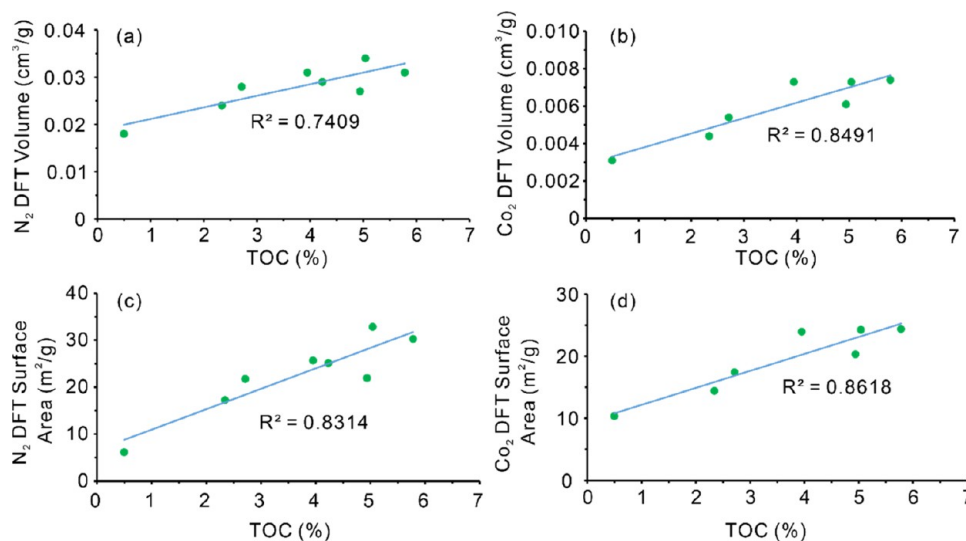


Figure 13. Relationships between TOC content and pore characteristics. (a) Relationship between pore volume obtained from the N_2 adsorption experiment and TOC content. (b) Relationship between pore volume obtained from the CO_2 adsorption experiment and TOC content. (c) Relationship between pore SSA obtained from the N_2 adsorption experiment and TOC content. (d) Relationship between pore SSA obtained from the CO_2 adsorption experiment and TOC content. R^2 = correlation coefficient. Whether it is N_2 surface area and volume or CO_2 surface area and volume, all show a highly positive correlation with TOC content.

vapor pressure, while the isotherms are similar to H4 at the low and medium pressure, suggesting that all hysteresis loops for these samples are approaching mixtures of H3 and H4 types based on the IUPAC classification standard.⁴⁹ It can be found that the area of the hysteresis loop increases with TOC content, and the sample with a bigger hysteresis loop shows stronger gas adsorption capacity (Figure 11), which indicates that the TOC content may have a great impact on the pore development. The distribution of pore SSA and volume concerning pore width was calculated by the DFT model (Table 3), presented in differential distribution curves (Figure 12), which highlights the increase in pore volume with changes in pore size and identifies the major contributors to pore volume increment. The plot of dV/dW concerning W exhibits a unimodal distribution of pore widths of 2–8 nm, which means that the quantity of pores in this range is the most proportion of total pores. Besides, the contribution of pore volume decreases with the increase of pore width (Figure 12a), and the plot of dS/dW versus W shows similar results to the pore volume (Figure 12b). Particularly, sample 1 shows a different manner, the pore width becomes larger, but the pore structure parameters become smaller (Figure 12).

5. DISCUSSION

5.1. Morphology Maintenance of Pores under Overpressure in Deep Shale. It has been demonstrated that the pore shape changes with increasing compaction and becomes increasingly perpendicular to the direction of maximum stress.²³ However, we still observed a large number of OM-hosted pores with a nearly orbicular shape, as well as inorganic pores (Figures 5 and 8). OM pores have a shape from ellipsoids to almost spherical with a smooth borderline, though the inner wall of these pores is rather rough (Figures 5l and 7a,b). At a larger scale, the OM is aggregated and dispersed in the matrix grains in clusters with numerous micropores (Figure 5a,d,g,j). However, at higher magnification and increased resolution, many pore shapes tend to show more increased rugosity (Figures 5l, 6c,i, and 7a,b,h). One of which has a sponge-like mesh interior (Figure 7b) that may increase pores' SSA and methane adsorption sites. OM, as compressible particles, can still maintain a low aspect ratio pore morphology in part of OM-hosted pores in deep shale reservoirs under enormous overlying pressure. The only explanation is the internal overpressure support, which protects OM-hosted pores from collapse. The shape of pores hosted by the mineral matrix is generally irregular

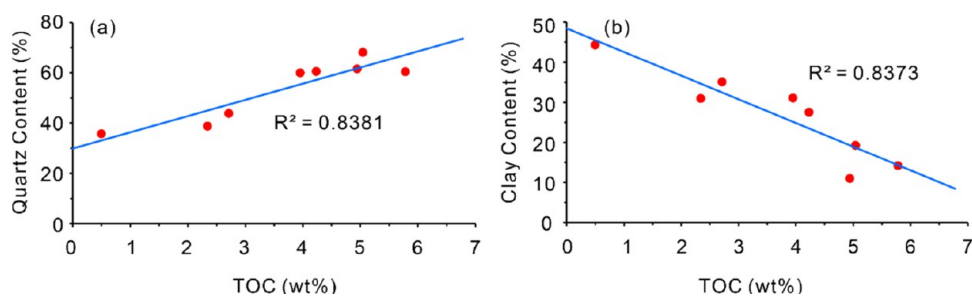


Figure 14. Relationships between quartz, clay, and TOC content. (a) Relationship between quartz content and TOC content. (b) Relationship between clay content and TOC content. R^2 = correlation coefficient. Quartz shows a positive correlation with TOC content; in contrast, clay minerals show a negative correlation with TOC content.

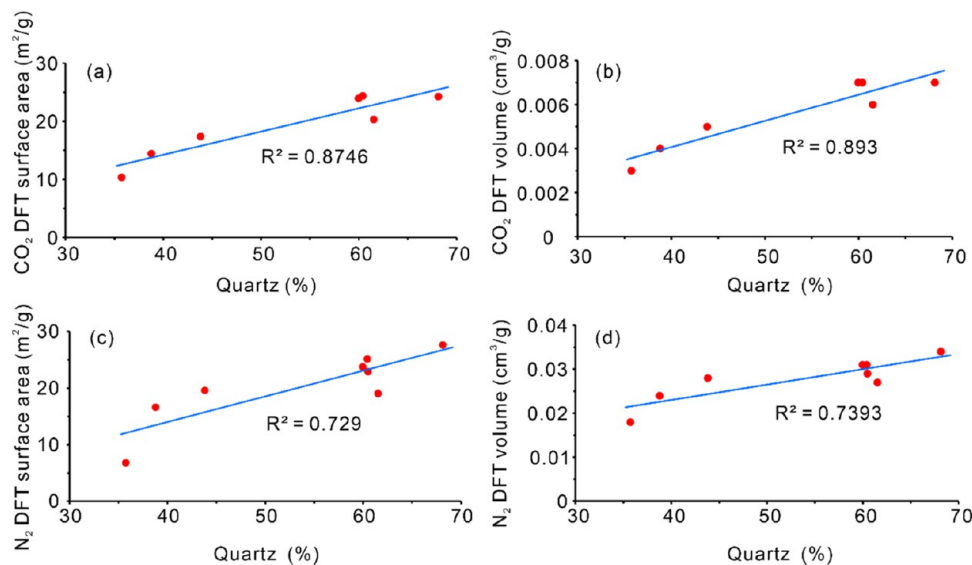


Figure 15. Relationships between pore structure parameters and quartz content. (a) Relationship between pore SSA obtained from the CO₂ adsorption experiment and the quartz content. (b) Relationship between pore volume obtained from the CO₂ adsorption experiment and the quartz content. (c) Relationship between pore SSA obtained from the N₂ adsorption experiment and the quartz content. (d) Relationship between pore volume obtained from the N₂ adsorption experiment and the quartz content. R^2 = correlation coefficient. Both pore volumes and surface areas show a positive correlation with quartz, which coincides with the result of the relationship between quartz and TOC.

polygonal with a straight borderline except for those pores with an almost circular shape (Figure 8a,e,f). This seems to prove that rigid grains act as part of the rock skeleton to protect the mineral-related pores. On the contrary, the shape of pores within clay minerals commonly occurred as slits or plates. The twisted slit pores associated with clay minerals are related to the deformation of illite or chlorite after compaction (Figure 8b,d,g,i), lying between rigid minerals.¹⁷ Although the cracks in clays seem to be elongated, the gas adsorption isotherms show few contributions of the cracks in clays to the pore volumes and surface areas (Figures 10a,b and 12a,b). The pores related to clays are affected by compaction from the beginning of burial; therefore, subsequent hydrocarbon generation can only maintain the morphology of the generated pores, and it is difficult to change the morphology of these pores.

The pore size varies dramatically from a few nanometers to several micrometers. According to the result of FE-SEM images, intraP pores and honeycombed OM pores are the smallest, and when the slit pores within clay minerals are not considered, OM pores have the biggest size (e.g., the largest pore width). The image-based porosity increases with TOC content (Table 2), but the maximum pore width is independent of TOC content. Such results may be related to the randomness of sample

selection. It is worth noting that macropores developed well in deep shale even under strong compaction, which may be related to preservation conditions with overpressure (pressure coefficient over 2), that prevent compaction and collapse of the OM pores, resulting in macropores in the micron scale serving as storage.^{13,24} The morphology of pores in the Luzhou area is similar to those in the Jiaoshiba shale.³⁸ OM pores, intraP pores, and interP pores were observed in the Luzhou area and also developed in the shallower shale of the Jiaoshiba area. The only difference is that the OM pores with micron size are observed in the Luzhou area, which is most likely due to overpressure protection,²⁴ but relatively smaller OM pores are developed in the Jiaoshiba area. This phenomenon is also confirmed in gas adsorption experiments, which are discussed in Section 5.3.

5.2. Influence of TOC and Petrography on Pore SSA and Volume under Overpressure. Published research has pointed out that TOC content dramatically affects the pore systems,^{17,22,29,51} and the study in this paper confirms this point as well. Both the pore volumes and SSA increase with TOC content (Figure 13), especially the volume and surface area of micropores (Figure 13b,d). The correlation coefficients between micropore structure parameters and TOC content indicate that the OM content had a greater impact on the development of

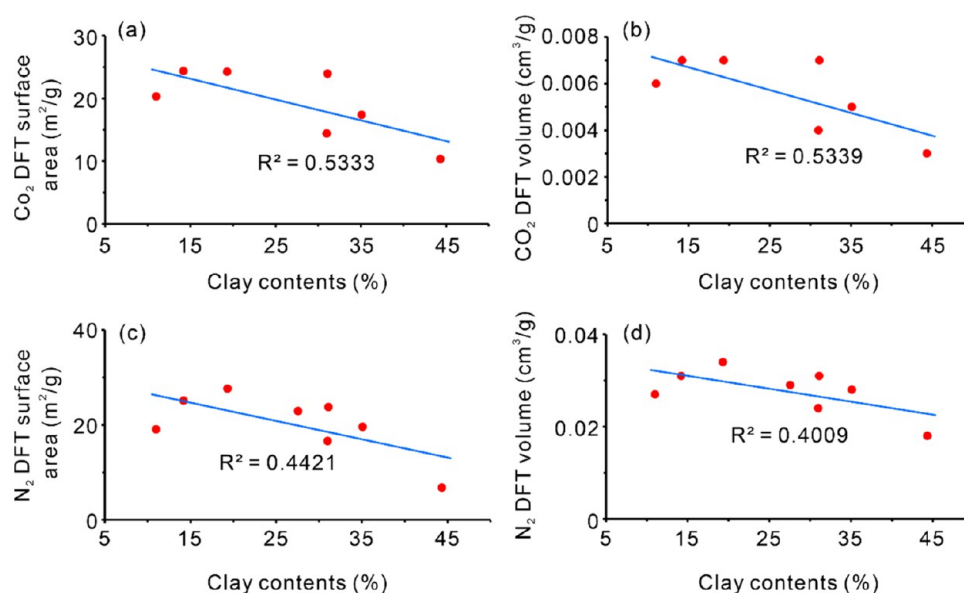


Figure 16. Relationships between pore structure parameters and clay content. (a) Relationship between pore SSA obtained from CO₂ adsorption experiment calculated by DFT. (b) Relationship between pore volume obtained from CO₂ adsorption experiment calculated by DFT. (c) Relationship between pore SSA obtained from N₂ adsorption experiment calculated by DFT. (d) Relationship between pore volume obtained from N₂ adsorption experiment calculated by DFT. R^2 = correlation coefficient. Both pore volumes and surface areas show a negative correlation with clay minerals, which also coincides with the result of the relationship between clay and TOC.

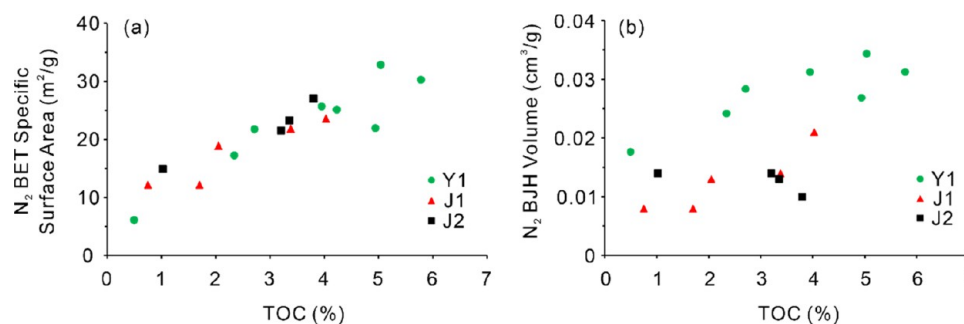


Figure 17. Relationships between pore structure parameters obtained from N₂ adsorption and TOC content. (a) The relationship between N₂ BET SSA and TOC content. (b) The relationship between N₂ BJH volume and TOC content. The pores in the overpressure area seem to own a larger pore volume than that in lower pressure.

micropores, which coincides with the result from FE-SEM. We found numerous OM micropores developed within OM at high magnification, some of them are so small even the FE-SEM cannot recognize them, leaving only a small black spot (Figures 5f, 6i, and 7f). According to the FE-SEM images, the size of OM pores ranges widely, from unidentifiable nanometers to micrometers. That is, OM pores do predominate the whole pores in deep shale, which once again confirmed the gas adsorption results.

It has been reported that quartz developed in Wufeng–Longmaxi siliceous shale is mainly derived from siliceous organisms.⁵² In this work, the quartz content increases with TOC content (Figure 14a), which also demonstrates the viewpoint that quartz in studied shale samples is dominated by biogenic quartz. Therefore, the quartz contents have a positive correlation with pore surface and volume (Figure 15), probably not because the mineral of quartz contributes to the pore characteristics but due to the biogenesis of quartz. Meanwhile, quartz is served as rigid grain, which can provide a good capacity to resist compaction, resulting in preserved interparticle pores.

The relationship between pore structure parameters and quartz content is similar to earlier studies in shale.^{17,29}

Pore parameters (pore volume and SS), however, are weakly negatively correlated with clay minerals (Figure 16); this result also coincides with the earlier study.^{29,37} Figure 12 shows that the peaks of dS/dW and dV/dW of sample 1 move forward with bigger pore width. Also, the total pore volume and SSA of sample 1 with the largest clay minerals are lower than others. That is, pores associated with clay minerals mainly contribute to mesopores, but few to total volume due to strong compaction.

All in all, OM has the greatest impact on the pore system of deep shale, and clay minerals have less impact. All evidence indicates that most pores formed in deep shale are related to OM. For example, high TOC content in Wufeng–Longmaxi shale generally means high silicon content derived from biogenesis and well-developed pyrite, which also means strong resistance to compaction, and numerous pores between these rigid grains can be preserved during diagenesis.² High TOC content within overmature deep shale means more dissolutive pores due to organic acids generated in the pyrolysis of OM dissolving unstable minerals. In addition, the proportion of

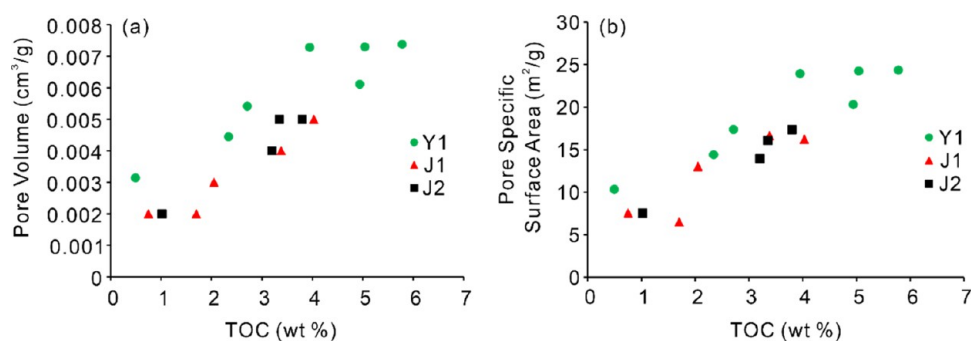


Figure 18. Relationships between pore structure parameters obtained from the CO₂ adsorption isotherm and TOC content. (a) The relationship between pore volume and the abundance of TOC. (b) The relationship between pore SSA and TOC content. The micropores in the overpressure area own larger pore volume and surface area than those in lower pressure.

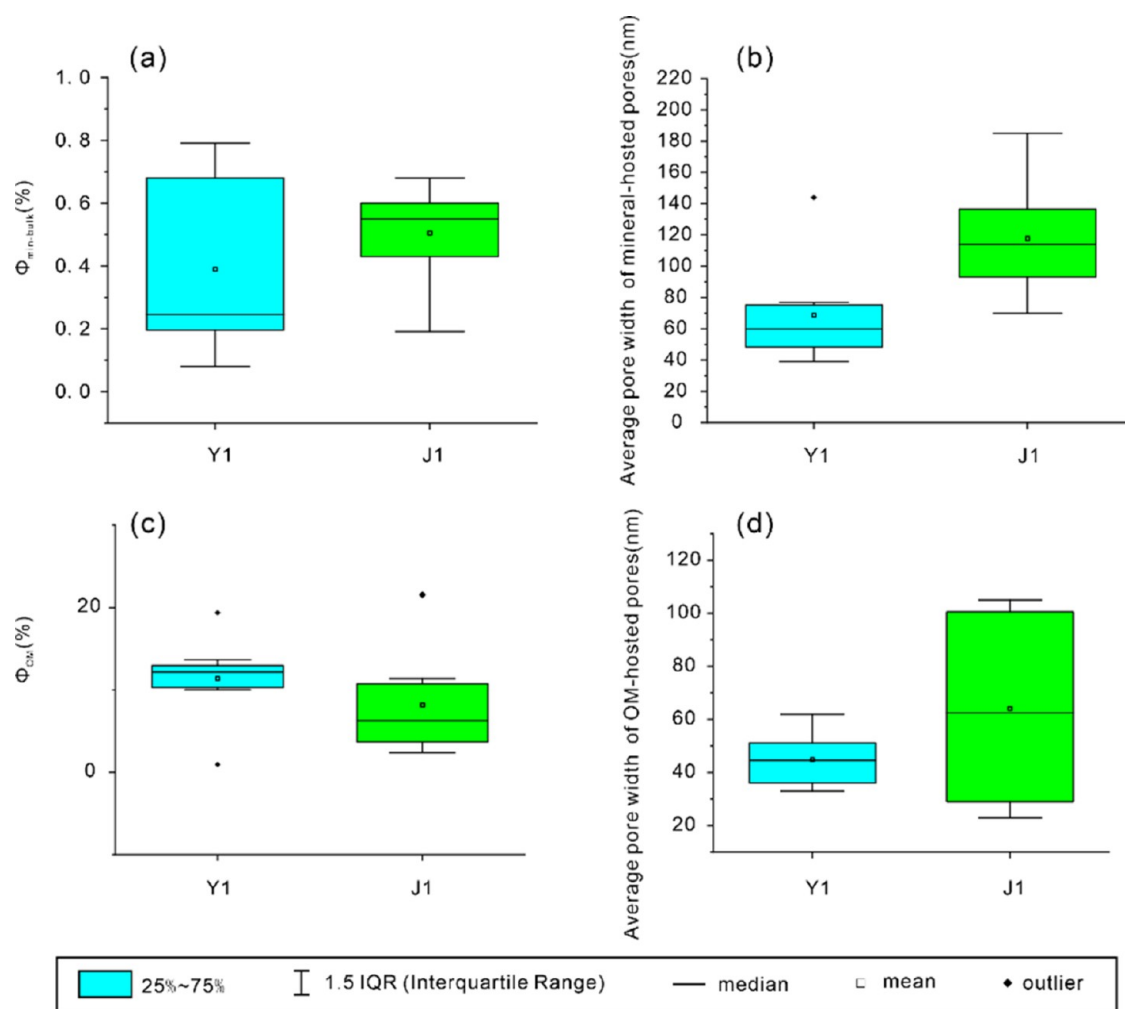


Figure 19. Box plots of porosity and pore width based on FE-SEM images. (a) Inorganic porosity in the bulk rock measured by FE-SEM for wells Y1 and J1; (b) average pore width of mineral-hosted pores for wells Y1 and J1; (c) OM-hosted porosity detected by FE-SEM for wells Y1 and J1; and (d) average pore width of OM-hosted pores for wells Y1 and J1.

dissolved pores increases with the carbonate content (e.g., samples 8 and 4), while the OM pores increase with high TOC content (e.g., samples 7, 6, and 5). A great amount of gas expelled during the pyrolysis of OM forms overpressure that can also protect pores.

5.3. Variation of Pore Characteristics under Overpressure. To ensure the accuracy of the conclusion, we have selected the pore characteristic parameters from the same model

for comparison. Gas adsorption data for Jiaoshiba shale was obtained from Yang et al.,³⁸ while the image-based pore size and porosity were obtained from Hu et al.^{17,39} (Table 2). The Jiaoshiba shale samples were taken from a buried depth range of 2303.64–2411.90 m with a pressure coefficient of 1.55.³⁸ The N₂ BET SSA of pores in the Luzhou area is similar to that in the Jiaoshiba area when TOC content is constant, although the pore volume exhibits different characteristics (Figure 17). Under the

condition of constant TOC content, the pore volume is observed to be bigger in the Luzhou area, indicating that overpressure significantly affects pore preservation when the other conditions remain constant. The characteristics of CO₂ adsorption also differ between Jiaoshiba shale and Luzhou shale. Although both exhibit multimodal distributions of pore volume and surface area, the width ranging from 0.4 to 0.7 nm appears to be bimodal in Jiaoshiba shale, while it tends to exhibit a single maximum value in Luzhou shale (Yang,⁵ Figure 9; Xu,²⁴ Figure 7; Gou,⁵³ Figure Sb), resulting in larger pore volume and SSA values for the same TOC content (Figure 18a). Besides, the range of inorganic porosity based on FE-SEM images in the two wells is similar (Figure 19). The deep shale in the Luzhou area is more developed with OM-hosted pores, and its OM-hosted porosity is higher than that in the Jiaoshiba area (Figure 18c). However, the average pore size of both OM-hosted and mineral-hosted pores in the Jiaoshiba area is higher than that in the Luzhou area, except for individual OM-hosted pores with larger pore sizes (Table 2), which seems to mean that deep shale has widely developed OM-hosted pores but generally has smaller width to resist stronger compaction (Figure 18b,d).


Overall, it appears that overpressure is the primary factor responsible for the differences in shale pore structures between the Jiaoshiba area and the Luzhou area. This overpressure condition significantly impacts the pore volume through the process of resistant compaction.

6. CONCLUSIONS

Certain OM-hosted pores maintain a near-circular shape under overpressure, while pore morphology related to hard minerals remains unaffected. Compaction causes elongated strip-like pore morphology in clay minerals. Mesoporous volume and pore SSA are determined by OM, but not micropores. Overpressure plays an important role in preserving pores, especially in deep shale, where gas generated by OM helps support and protect them from collapse. Deeper shale can have a large pore volume than shallower shale due to overpressure.

AUTHOR INFORMATION

Corresponding Authors

Renfang Pan – School of Geosciences, Yangtze University, Wuhan 430100, China; Key Laboratory of Exploration Technologies for Oil and Gas Resources, Ministry of Education, Yangtze University, Wuhan 430100, China;  orcid.org/0000-0003-2727-1743; Email: pan@yangtzeu.edu.cn

Haiyan Hu – Hubei Key Laboratory of Petroleum Geochemistry and Environment, Yangtze University, Wuhan 430100, China; Email: hyhucom@163.com

Authors

Lingling Xu – School of Geosciences, Yangtze University, Wuhan 430100, China; Key Laboratory of Exploration Technologies for Oil and Gas Resources, Ministry of Education, Yangtze University, Wuhan 430100, China

Tao Wang – School of Geosciences, Yangtze University, Wuhan 430100, China

Complete contact information is available at:
<https://pubs.acs.org/10.1021/acsomega.3c03351>

Notes

The authors declare no competing financial interest.

ACKNOWLEDGMENTS

The authors would like to thank PetroChina Southwest Oil & Gas field Company for providing core samples. This work was supported by the National Natural Science Foundation of China (Grant Number 41472123).

REFERENCES

- (1) Ma, X.; Wang, H.; Zhou, S.; Shi, Z.; Zhang, L. Deep shale gas in China: geological characteristics and development strategies. *Energy Rep.* **2021**, *7*, 1903–1914.
- (2) Chen, Y.; Xu, J.; Wang, P. Shale gas potential in China: a production forecast of the Wufeng-Longmaxi Formation and implications for future development. *Energy Policy* **2020**, *147*, No. 111868.
- (3) Li, S.; Zhou, Z.; Nie, H.; Zhang, L.; Song, T.; Liu, W.; Li, H.; Xu, Q.; Wei, S.; Tao, S. Distribution characteristics, exploration and development, geological theories research progress and exploration directions of shale gas in China. *China Geol.* **2022**, *5*, 110–135.
- (4) Zhang, L.; He, X.; Li, X.; Li, K.; He, J.; Zhang, Z.; Guo, J.; Chen, Y.; Liu, W. Shale gas exploration and development in the Sichuan Basin: Progress, challenge and countermeasures. *Nat. Gas Ind. B* **2022**, *9*, 176–186.
- (5) Yang, H.; Zhao, S.; Liu, Y.; Wu, W.; Xia, Z.; Wu, T.; Luo, C.; Fan, T.; Yu, L. Main controlling factors of enrichment and high-yield of deep shale gas in the Luzhou Block, southern Sichuan Basin. *Nat. Gas Ind.* **2019**, *39*, 55–63.
- (6) Loucks, R. G.; Reed, R. M.; Ruppel, S. C.; Hammes, U. Spectrum of pore types and networks in mudrocks and a descriptive classification for matrix-related mudrock pores. *AAPG Bull.* **2012**, *96*, 1071–1098.
- (7) Ross, D. J. K.; Bustin, R. M. The importance of shale composition and pore structure upon gas storage potential of shale gas reservoirs. *Mar. Pet. Geol.* **2009**, *26*, 916–927.
- (8) Yang, R.; Hao, F.; He, S.; He, C.; Guo, X.; Yi, J.; Hu, H.; Zhang, S.; Hu, Q. Experimental investigations on the geometry and connectivity of pore space in organic-rich Wufeng and Longmaxi Shales. *Mar. Pet. Geol.* **2017**, *84*, 225–242.
- (9) Teng, J.; Liu, B.; Mastalerz, M.; Schieber, J. Origin of organic matter and organic pores in the overmature Ordovician-Silurian Wufeng-Longmaxi Shale of the Sichuan Basin, China. *Int. J. Coal Geol.* **2022**, *253*, No. 103970.
- (10) Milliken, K. L.; Esch, W. L.; Reed, R. M.; Zhang, T. Grain assemblages and strong diagenetic overprinting in siliceous mudrocks, Barnett Shale (Mississippian), Fort Worth Basin, Texas. *AAPG Bull.* **2012**, *96*, 1553–1578.
- (11) Han, C.; Jiang, Z.; Han, M.; Wu, M.; Lin, W. The lithofacies and reservoir characteristics of the Upper Ordovician and Lower Silurian black shale in the Southern Sichuan Basin and its periphery. *China. Mar. Pet. Geol.* **2016**, *75*, 181–191.
- (12) Wang, Y.; Cheng, H.; Hu, Q.; Liu, L.; Jia, L.; Gao, S.; Wang, Y. Pore structure heterogeneity of Wufeng-Longmaxi shale, Sichuan Basin, China: Evidence from gas physisorption and multifractal geometries. *J. Pet. Sci. Eng.* **2022**, *208*, No. 109313.
- (13) Milliken, K. L.; Rudnicki, M.; Awwiller, D. N.; Zhang, T. Organic matter-hosted pore system, Marcellus Formation (Devonian), Pennsylvania. *AAPG Bull.* **2013**, *97*, 177–200.
- (14) Wang, X.; Liu, L.; Wang, Y.; Sheng, Y.; Zheng, S.; Wu, W.; Luo, Z. Comparison of the pore structures of Lower Silurian Longmaxi Formation shales with different lithofacies in the southern Sichuan Basin, China. *J. Nat. Gas Sci. Eng.* **2020**, *81*, No. 103419.
- (15) Wang, Y.; Cheng, H.; Hu, Q.; Liu, L.; Hao, L. Diagenesis and pore evolution for various lithofacies of the Wufeng-Longmaxi shale, southern Sichuan Basin, China. *Mar. Pet. Geol.* **2021**, *133*, No. 105251.
- (16) He, S.; Li, H.; Qin, Q.; Long, S. Influence of mineral compositions on shale pore development of Longmaxi Formation in the Dingshan Area, Southeastern Sichuan Basin, China. *Energy Fuels* **2021**, *35*, 10551–10561.
- (17) Hu, H.; Hao, F.; Guo, X.; Yi, J.; Shu, Z.; Bao, H.; Zhu, X. Effect of lithofacies on the pore system of over-mature Longmaxi shale in the

- Jiaoshiba area, Sichuan Basin, China. *Mar. Pet. Geol.* **2019**, *109*, 886–898.
- (18) Chen, L.; Jiang, Z.; Liu, K.; Wang, P.; Ji, W.; Gao, F.; Li, P.; Hu, T.; Zhang, B.; Huang, H. Effect of lithofacies on gas storage capacity of marine and continental shales in the Sichuan Basin, China. *J. Nat. Gas Sci. Eng.* **2016**, *36*, 773–785.
- (19) Iqbal, O.; Padmanabhan, E.; Mandal, A.; Dvorkin, J. Characterization of geochemical properties and factors controlling the pore structure development of shale gas reservoirs. *J. Pet. Sci. Eng.* **2021**, *206*, No. 109001.
- (20) Zhao, J.; Jin, Z.; Hu, Q.; Liu, K.; Jin, Z.; Hu, Z.; Nie, H.; Du, W.; Yan, C.; Wang, R. Mineral composition and seal condition implicated in pore structure development of organic-rich Longmaxi shales, Sichuan Basin, China. *Mar. Pet. Geol.* **2018**, *98*, 507–522.
- (21) Guo, X.; Qin, Z.; Yang, R.; Dong, T.; He, S.; Hao, F.; Yi, J.; Shu, Z.; Bao, H.; Liu, K. Comparison of pore systems of clay-rich and silica-rich gas shales in the lower Silurian Longmaxi formation from the Jiaoshiba area in the eastern Sichuan Basin, China. *Mar. Pet. Geol.* **2019**, *101*, 265–280.
- (22) Ji, W.; Hao, F.; Schulz, H. M.; Song, Y.; Tian, J. The architecture of organic matter and its pores in highly mature gas shales of the lower Silurian Longmaxi Formation in the upper Yangtze platform, south China. *AAPG Bull.* **2019**, *103*, 2909–2942.
- (23) Yang, Y.; Aplin, A. C. Influence of lithology and compaction on the pore size distribution and modelled permeability of some mudstones from the Norwegian margin. *Mar. Pet. Geol.* **1998**, *15*, 163–175.
- (24) Xu, S.; Gou, Q.; Hao, F.; Zhang, B.; Shu, Z.; Lu, Y.; Wang, Y. Shale pore structure characteristics of the high and low productivity wells, Jiaoshiba shale gas field, Sichuan Basin, China: Dominated by lithofacies or preservation condition? *Mar. Pet. Geol.* **2020**, *114*, No. 104211.
- (25) Guo, X.; Hu, D.; Li, Y.; Wei, Z.; Wei, X.; Liu, Z. Geological factors controlling shale gas enrichment and high production in Fuling shale gas field. *Pet. Explor. Dev.* **2017**, *44*, 513–523.
- (26) Gao, J.; Zhang, J.; He, S.; Zhao, J.; He, Z.; Wo, Y.; Feng, Y.; Li, W. Overpressure generation and evolution in Lower Paleozoic gas shales of the Jiaoshiba region, China: Implications for shale gas accumulation. *Mar. Pet. Geol.* **2019**, *102*, 844–859.
- (27) Liu, S.; Jiao, K.; Zhang, J.; Ye, Y.; Xie, G.; Deng, B.; Ran, B.; Li, Z.; Wu, J.; Li, J.; Liu, W.; Luo, C. Research progress on the pore characteristics of deep shale gas reservoirs: An example from the Lower Paleozoic marine shale in the Sichuan Basin. *Nat. Gas Ind.* **2021**, *41*, 29–41.
- (28) Liu, R. Analyses of influences on shale reservoirs of Wufeng-Longmaxi Formation by overpressure in the South-eastern Part of Sichuan Basin. *Acta Sedimentol. Sin.* **2015**, *33*, 817–827.
- (29) Hu, H.; Hao, F.; Lin, J.; Lu, Y.; Ma, Y.; Li, Q. Organic matter-hosted pore system in the Wufeng-Longmaxi (O3w-S11) shale, Jiaoshiba area, Eastern Sichuan Basin, China. *Int. J. Coal Geol.* **2017**, *173*, 40–50.
- (30) Qiu, L.; Yan, D.; Tang, S.; Chen, F.; Song, Z.; Gao, T.; Zhang, Y. Insights into post-orogenic extension and opening of the Palaeo-Tethys Ocean recorded by an Early Devonian core complex in South China. *J. Geodyn.* **2020**, *135*, No. 101708.
- (31) Wang, H.; Shi, Z.; Sun, S. Biostratigraphy and reservoir characteristics of the Ordovician Wufeng Formation—Silurian Longmaxi Formation shale in the Sichuan Basin and its surrounding areas, China. *Pet. Explor. Dev.* **2021**, *48*, 1019–1032.
- (32) Li, Y.; He, D.; Chen, L.; Mei, Q.; Li, C.; Zhang, L. Cretaceous sedimentary basins in Sichuan, SW China: Restoration of tectonic and depositional environments. *Cretaceous Res.* **2016**, *57*, 50–65.
- (33) Nie, H.; Jin, J.; Ma, X.; Liu, Z.; Lin, T.; Yang, Z. Graptolites zone and sedimentary characteristics of Upper Ordovician Wufeng Formation-Lower Silurian Longmaxi Formation in Sichuan Basin and its adjacent area. *Acta Pet. Sin.* **2017**, *38*, 160–174.
- (34) Liu, S.; Deng, B.; Zhong, Y.; Ran, B.; Yong, Z.; Sun, W.; Yang, D.; Jiang, L.; Ye, Y. Unique geological features of burial and superimposition of the Lower Paleozoic shale gas across the Sichuan Basin and its periphery. *Earth Sci. Front.* **2016**, *23*, 11–28.
- (35) Su, G.; Li, Z.; Ying, D.; Li, G.; Ying, W.; Yang, Y.; Liu, H.; Ding, X.; Tang, H. Formation and evolution of the Caledonian paleo-uplift and its genetic mechanism in the Sichuan Basin. *Acta Geol. Sin.* **2020**, *94*, 1793–1812.
- (36) Zhu, Y.; Chen, G.; Liu, Y.; Shi, X.; Wu, W.; Luo, C.; Yang, X.; Yang, Y.; Zou, Y. Sequence stratigraphy and lithofacies paleogeographic evolution of Katian Stage – Aeronian Stage in southern Sichuan Basin, SW China. *Pet. Explor. Dev.* **2021**, *48*, 1126–1138.
- (37) Yang, R.; He, S.; Yi, J.; Hu, Q. Nano-scale pore structure and fractal dimension of organic-rich Wufeng-Longmaxi shale from Jiaoshiba area, Sichuan Basin: Investigations using FE-SEM, gas adsorption and helium pycnometry. *Mar. Pet. Geol.* **2016**, *70*, 27–45.
- (38) Schmidt, J. S.; Menezes, T. R.; Souza, I. V. A. F.; Spigolon, A. L. D.; Pestilho, A. L. S.; Coutinho, L. F. C. Comments on empirical conversion of solid bitumen reflectance for thermal maturity evaluation. *Int. J. Coal Geol.* **2019**, *201*, 44–50.
- (39) Hu, H.; Hao, F.; Guo, X.; Dai, F.; Lu, Y.; Ma, Y. Investigation of methane sorption of overmature Wufeng-Longmaxi shale in the Jiaoshiba area, Eastern Sichuan Basin, China. *Mar. Pet. Geol.* **2018**, *91*, 251–261.
- (40) Brunauer, S.; Emmett, P. H.; Teller, E. Adsorption of gases in multimolecular layer. *J. Am. Chem. Soc.* **1938**, *60*, 309–319.
- (41) Barrett, E. P.; Joyner, L. G.; Halenda, P. P. The determination of pore volume and area distributions in porous substances. I. Computations from nitrogen isotherms. *J. Am. Chem. Soc.* **1951**, *73*, 373–380.
- (42) Odoh, S. O.; Cramer, C. J.; Truhlar, D. G.; Gagliardi, L. Quantum-Chemical Characterization of the Properties and Reactivities of metal-organic frameworks. *Chem. Rev.* **2015**, *115*, 6051–6111.
- (43) Yu, J.; Xie, L. H.; Li, J. R.; Ma, Y.; Seminario, J. M.; Balbuena, P. B. CO₂ capture and separations using MOFs: computational and experimental studies. *Chem. Rev.* **2017**, *117*, 9674–9754.
- (44) Gregg, S. J.; Sing, K. S. W. *Adsorption, Surface Area and Porosity*; Academic Press: New York, 1982; p 303.
- (45) Ravikovitch, P. I.; Neimark, A. V. Density functional theory model of adsorption on amorphous and microporous silica materials. *Langmuir* **2006**, *22*, 11171–11179.
- (46) Yang, R.; Jia, A.; He, S.; Hu, Q.; Sun, M.; Dong, T.; Hou, Y.; Zhou, S. Experimental investigation of water vapor adsorption isotherm on gas-producing Longmaxi shale: Mathematical modeling and implication for water distribution in shale reservoirs. *Chem. Eng. J.* **2021**, *406*, No. 125982.
- (47) Slatt, R. M.; O'Brien, N. R. Pore types in the Barnett and Woodford gas shales: Contribution to understanding gas storage and migration pathways in fine-grained rocks. *AAPG Bull.* **2011**, *95*, 2017–2030.
- (48) Ko, L. T.; Ruppel, S. C.; Loucks, R. G.; Hackley, P. C.; Zhang, T.; Shao, D. Pore-types and pore-network evolution in Upper Devonian-Lower Mississippian Woodford and Mississippian Barnett mudstones: Insights from laboratory thermal maturation and organic petrology. *Int. J. Coal Geol.* **2018**, *190*, 3–28.
- (49) Thommes, M.; Kaneko, K.; Neimark, A. V.; Olivier, J. P.; Rodriguez-Reinoso, F.; Rouquerol, J.; Sing, K. S. W. Physisorption of gases, with special reference to the evaluation of surface area and pore size distribution (IUPAC Technical Report). *Pure Appl. Chem.* **2015**, *87*, 1051–1069.
- (50) Groen, J. C.; Peffer, L. A. A.; Pérez-Ramírez, J. Pore size determination in modified micro- and mesoporous materials. Pitfalls and limitations in gas adsorption data analysis. *Microporous Mesoporous Mater.* **2003**, *60*, 1–17.
- (51) Tian, H.; Pan, L.; Xiao, X.; Wilkins, R. W. T.; Meng, Z.; Huang, B. A preliminary study on the pore characterization of Lower Silurian black shales in the Chuandong Thrust Fold Belt, southwestern China using low pressure N₂ adsorption and FE-SEM methods. *Mar. Pet. Geol.* **2013**, *48*, 8–19.
- (52) Ye, Y.; Tang, S.; Xi, Z.; Jiang, D.; Duan, Y. Quartz types in the Wufeng-Longmaxi Formations in southern China: Implications for

porosity evolution and shale brittleness. *Mar. Pet. Geol.* **2022**, *137*, No. 105479.

(53) Gou, Q.; Xu, S.; Hao, F.; Yang, F.; Zhang, B.; Shu, Z.; Zhang, A.; Wang, Y.; Lu, Y.; Cheng, X.; Qing, J.; Gao, M. Full-scale pores and micro-fractures characterization using FE-SEM, gas adsorption, nano-CT and micro-CT: A case study of the Silurian Longmaxi Formation shale in the Fuling area, Sichuan Basin, China. *Fuel* **2019**, *253*, 167–179.